Materials Screening for Disorder-Controlled Chalcogenide Crystals for Phase-Change Memory Applications

Yazhi Xu, Xudong Wang, Wei Zhang,* Lisa Schäfer, Johannes Reindl, Felix vom Bruch, Yuxing Zhou, Valentin Evang, Jiang-Jing Wang, Volker L. Deringer, En Ma, Matthias Wuttig,* and Riccardo Mazzarello*

Tailoring the degree of disorder in chalcogenide phase-change materials (PCMs) plays an essential role in nonvolatile memory devices and neuro-inspired computing. Upon rapid crystallization from the amorphous phase, the flagship Ge–Sb–Te PCMs form metastable rocksalt-like structures with an unconventionally high concentration of vacancies, which results in disordered crystals exhibiting Anderson-insulating transport behavior. Here, ab initio simulations and transport experiments are combined to extend these concepts to the parent compound of Ge–Sb–Te alloys, viz., binary Sb_2Te_3, in the metastable rocksalt-type modification. Then a systematic computational screening over a wide range of homologous, binary and ternary chalcogenides, elucidating the critical factors that affect the stability of the rocksalt structure is carried out. The findings vastly expand the family of disorder-controlled main-group chalcogenides toward many more compositions with a tunable bandgap size for demanding phase-change applications, as well as a varying strength of spin–orbit interaction for the exploration of potential topological Anderson insulators.

The seminal paper by Anderson on disorder-induced insulating behavior[1] sparked a new field of research which, 60 years later, is still thriving. Anderson showed that for a random model Hamiltonian with on-site disorder, no diffusion can occur because all the electronic states are localized. Ten years later, Mott introduced the concept of the mobility edge for generic random Hamiltonians: by definition, the mobility edge separates extended states from localized ones.[2] In this more general case, insulating behavior occurs at zero temperature when the Fermi level, E_F, lies in the region of localized states. Subsequently, Anderson and co-workers proposed the scaling theory of localization,[3] according to which all electronic states are localized in 1D and 2D disordered systems, irrespective of the strength of randomness, as long as electron correlations and spin–orbit coupling are weak. In contrast, 3D systems can undergo a metal–insulator transition (MIT)[2] upon changing disorder or tuning E_F across the mobility edge. Disorder-induced electron localization and MITs were extensively investigated in doped semiconductors,[4] such as phosphorus-doped silicon (Si:P) and aluminum-doped gallium arsenide ($Al_xGa_{1-x}As$).

Y. Xu, X. Wang, Prof. W. Zhang, Y. Zhou, Dr. J.-J. Wang, Prof. E. Ma
Center for Advancing Materials Performance from the Nanoscale
State Key Laboratory for Mechanical Behavior of Materials
Xi'an Jiaotong University
Xi'an 710049, China
E-mail: wzhang0@mail.xjtu.edu.cn

Y. Xu, V. Evang, Prof. R. Mazzarello[+]
Institute for Theoretical Solid-State Physics
JARA-FIT and JARA-HPC
RWTH Aachen University
52056 Aachen, Germany
E-mail: mazzarello@physik.rwth-aachen.de,
riccardo.mazzarello@uniroma1.it

The ORCID identification number(s) for the author(s) of this article can be found under https://doi.org/10.1002/adma.202006221.

X. Wang, Prof. W. Zhang, Y. Zhou, Prof. E. Ma
Center for Alloy Innovation and Design (CAID)
Materials Studio for Neuro-Inspired Computing
Xi'an Jiaotong University
Xi'an 710049, China

L. Schäfer, J. Reindl, F. vom Bruch, Dr. J.-J. Wang, Prof. M. Wuttig
I. Institute of Physics (IA)
JARA-FIT and JARA-HPC
RWTH Aachen University
52056 Aachen, Germany
E-mail: wuttig@physik.rwth-aachen.de

Prof. V. L. Deringer
Department of Chemistry
Inorganic Chemistry Laboratory
University of Oxford
Oxford OX1 3QR, UK

Prof. M. Wuttig
Peter Grünberg Institute (PGI 10)
Forschungszentrum Jülich GmbH
52425 Jülich, Germany

[+]Present address: Department of Physics, Sapienza University of Rome, 00185 Rome, Italy

Yet, it turned out that true disorder-induced localization of electrons in solids is more difficult to find than originally anticipated. This is because Anderson's theory is a one-electron theory, which has to be modified if strong electronic correlations prevail.[5–7] Since disorder inevitably increases electronic correlations it is very difficult to identify solids which present true disorder-induced localization of electronic states.[5–7] At present, photons, phonons, and ultracold atoms are explored to study Anderson localization.[8–12] To complicate matters further, besides disorder and correlations there are other effects which can localize electronic states: an example is given by phase transitions which open a bandgap.

Chalcogenide phase-change materials (PCMs) are employed in nonvolatile memory and neuro-inspired computing applications, which exploit the large difference in electrical resistivity or optical reflectivity between the amorphous (RESET) and crystalline (SET) state of PCMs.[13–19] Recently, disorder-driven insulator–metal transitions were observed in crystalline Ge–Sb–Te compounds along the GeTe–Sb_2Te_3 pseudo-binary line (such as $Ge_2Sb_2Te_5$ and $GeSb_2Te_4$), which form an important family of PCMs.[20–24] Upon nanosecond crystallization induced by electrical/optical pulses or thermal annealing (about 150–200 °C), Ge–Sb–Te alloys form an Anderson-insulating metastable rocksalt-like phase with a high concentration of randomly distributed atomic vacancies ($\approx$10%).[20] Higher annealing temperatures induce a phase transition to a stable, metallic phase. The two phases show similar bandgap size and carrier concentration, but a large contrast in carrier mobility and opposite temperature-dependence of the resistivity.[20] The microscopic origin of this transition is the ordering of vacancies into 2D vacancy planes.[21,25–30]

Anderson localization in vacancy-rich compounds was already investigated by Cutler and Mott in 1969, who showed that in Ce_2S_3, the random distribution of vacancies creates a tail of localized states in the conduction band, and that addition of a small number of cerium atoms per formula unit leads to a small number of electrons in the tail of the band and, thus, to insulating behavior.[31] More recently, Anderson localization effects were observed in rocksalt-like compounds chemically related to the abovementioned PCMs, including $SnBi_2Te_4$ and $SnSb_2Te_4$ thin films,[32,33] and also in GeTe nanowires.[34] In ref. [32], an isotropic positive magnetoconductivity was observed in the hopping regime of conductivity in $SnSb_2Te_4$ thin films. The magnetoconductivity was shown to increase with disorder, and was ascribed to the destruction of spin correlations and spin memory effects, i.e., spin-dependent hopping probabilities.[32] This raises the question why chalcogenides such as GeTe, Sb_2Te_3, or $GeSb_2Te_4$ seem to favor disorder-induced localization (rather than correlation effects).

Figure 1 summarizes the different microscopic mechanisms at play in these materials—here, focusing on the disordered phase of Sb_2Te_3, which contains a substantial number of Sb vacancies (Figure 1a). For a network of σ-bonds formed by the valence p-orbitals, illustrated in Figure 1b using a 1D band structure for simplicity, small distortions (Peierls distortion) are expected to open a bandgap. In this simplified picture, one would expect rocksalt-type Sb_2Te_3 to be a small-gap insulator. However, Sb_2Te_3, GeTe, $GeSb_2Te_4$, $SnBi_2Te_4$, and other chalcogenides often show metal-like electrical conductivity: this has been ascribed to self-doping effects, such as the presence of excess vacancies ($\approx$0.1%) on either the cation-like (p-type) or the anion-like sublattice (n-type), in addition to those vacancies that are already present based on the stoichiometric composition alone.[33,35–37] For p-type rocksalt chalcogenides, self-doping shifts E_F down into the valence band, typically about 0.1 eV below the upper valence band edge (Figure 1b,c). Furthermore, these materials are characterized by high values of the Born effective charge, leading to a large static dielectric constant[38] (which strongly reduces correlation effects), and by a competition between electron localization and delocalization.[39]
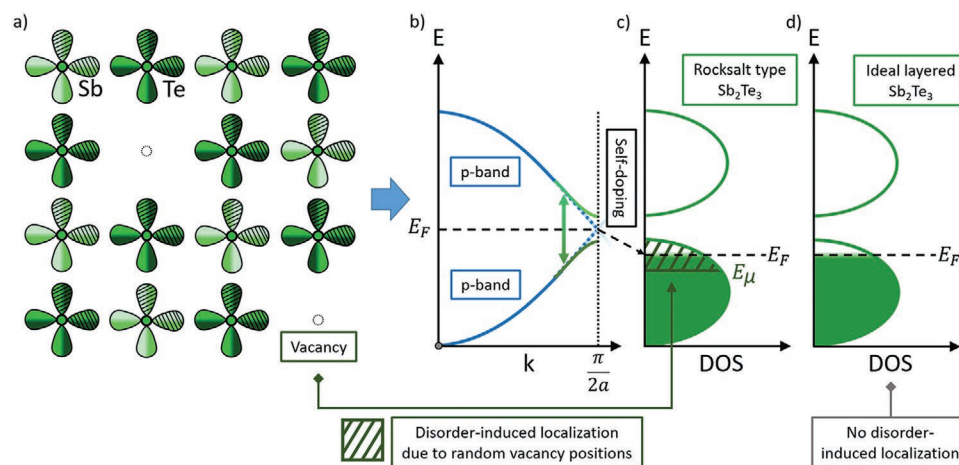
Figure 1. Schematic overview of aspects of the electronic structure in Sb_2Te_3 (and many related disordered chalcogenide materials). a) A 2D arrangement of Sb and Te atoms, representing the xy plane of a rocksalt-type structure, with two Sb sites being vacant (empty circles) and two p valence orbitals per atom indicated. b) Electronic band structure of a 1D σ-bonded chain of p-orbitals (i.e., oriented along the chain direction), indicating the opening of a small bandgap as a consequence of a Peierls distortion, and a Fermi level, E_F, corresponding to half-filled p-bands. "Self-doping", i.e., the removal of cations beyond the stoichiometric composition, shifts E_F downward into the valence band. c) Schematic density of states (DOS) for rocksalt-type Sb_2Te_3. The electronic states near the valence band maximum can become localized due to disorder (hatched region) caused by the random arrangement of vacancies as well as disordered lattice distortions. This effect is absent in the ordered, layered structure of rhombohedral Sb_2Te_3 (panel d), and therefore self-doping gives rise to metallic conduction in this case. a,b) Adapted with permission.[37] Copyright 2020, Wiley-VCH.

Together with high levels of distortions and vacancy disorder (Figure 1a), this leads to uniquely favorable conditions to observe disorder-induced localization.

The questions raised by disordered chalcogenide materials, both with regard to fundamental research and to technological applications, make it of interest to search for other compounds that can form strongly disordered (meta-)stable rocksalt-like phases with similar properties. In the present work, we therefore perform a systematic computational screening of rocksalt-like binary and ternary chalcogenide compounds, most of which have not been previously synthesized. We find that many of these phases can sustain large concentrations of vacancies by forming metastable rocksalt-like structures, and most exhibit disorder-induced insulating behavior.
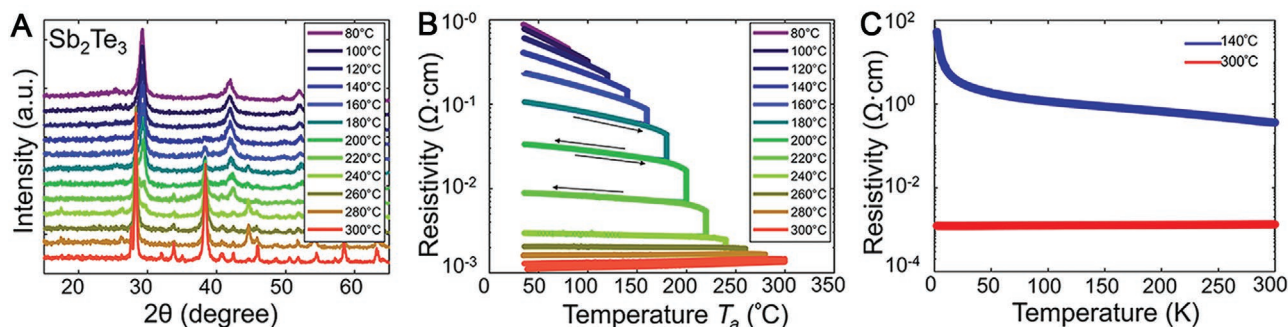
First, we focus on Sb_2Te_3, which was recently shown to become an ultrafast PCM when properly alloyed.[40] In addition to its stable layered rhombohedral phase, it forms a less widely studied, metastable rocksalt-type phase upon fast crystallization[40] or magnetron sputtering.[41] Scanning transmission electron microscopy experiments confirmed the presence of a large amount of atomic vacancies distributed in a random fashion on the cation-like sublattice of rocksalt Sb_2Te_3,[41] similar to rocksalt Ge–Sb–Te.[25] Here, we carry out density functional theory (DFT) simulations to shed light on why such disordered rocksalt structure exists. We construct $3 \times 3 \times 3$ supercell models of two rocksalt-like compounds, namely SbTe and Sb_2Te_3: in the former, all the sites of the cation-like sublattice are occupied by Sb atoms, while in the latter, only two of three cation sites are occupied and the remaining vacant sites are distributed randomly. The atomic structures, electronic densities of states (DOS), and the crystal orbital Hamilton population (COHP)[42] chemical-bonding analyses are presented in **Figure 2**A–D. Hypothetical rocksalt SbTe shows metallic behavior with strong antibonding character near E_F (Figure 2B), indicating chemical instability. Such antibonding character is sharply reduced by creating Sb vacancies, lowering the excess p electron count by 0.5 per site; therefore, no destabilizing contribution is present at E_F in rocksalt Sb_2Te_3 (Figure 2D). This trend in orbital interactions is consistent with the one displayed by rocksalt Ge–Sb–Te alloys,[43] which were recently shown to exhibit a peculiar bonding mechanism—namely, metavalent bonding (MVB)—that gives rise to the unconventional and application-relevant properties of these materials.[39,44–46]

We perform large-scale DFT calculations to assess the impact of atomic vacancies on the electronic structure of rocksalt Sb_2Te_3. A supercell with size $30.69 \times 30.37 \times 32.22$ Å^3, consisting of 840 atoms and 168 vacancies, is constructed to ensure a good statistical distribution of the vacancies. We compute the local density of p states (LDOS) of Te atoms, and group them according to their nearest-neighbor (NN)
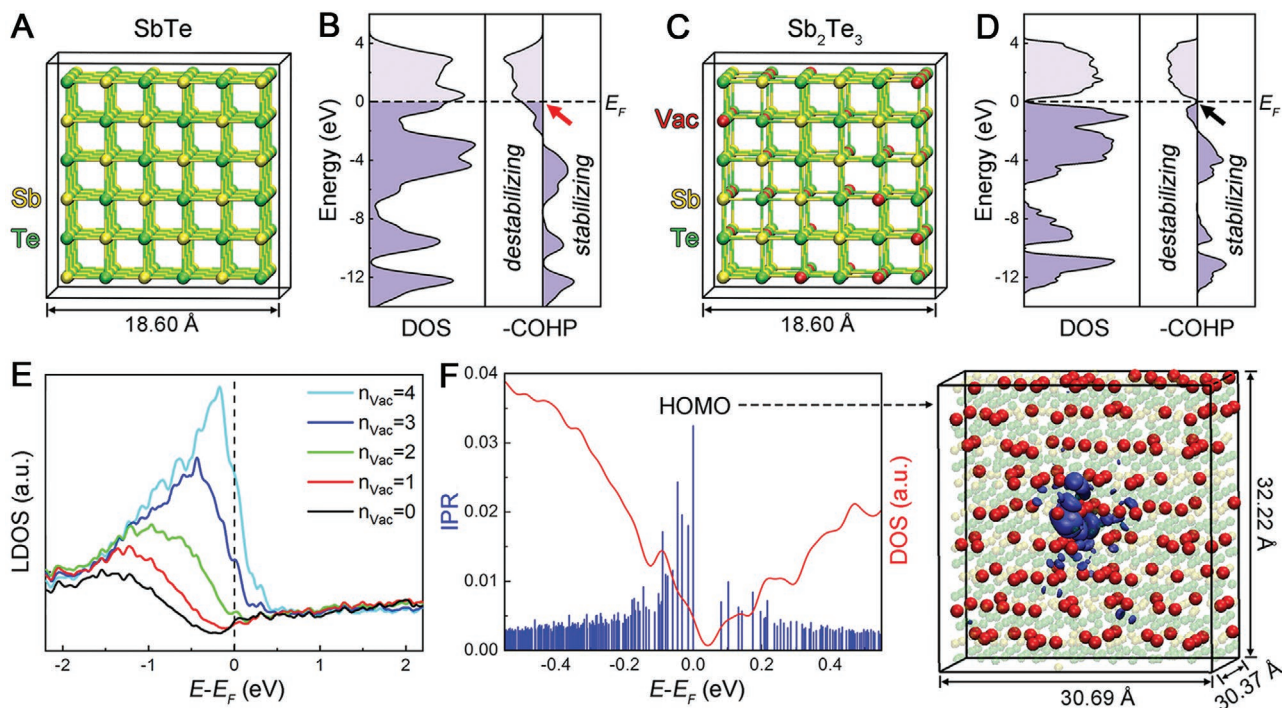
Figure 2. Electronic structure and bonding of rocksalt Sb–Te compounds. A) The atomic structure of the hypothetical SbTe model and B) its corresponding density of states (DOS) and crystal orbital Hamilton population (COHP) curve. The red arrow indicates the presence of antibonding interactions (–COHP < 0) at and near the Fermi level, E_F. C) The atomic structure of the unrelaxed rocksalt Sb_2Te_3. Atomic vacancies are randomly distributed in the cation-like sublattice. D) The DOS and COHP curves of rocksalt Sb_2Te_3 after full atomic relaxation (see also ref. [40]). The two cubic models use the same lattice parameter, $a = 6.20$ Å, corresponding to the equilibrium lattice parameter of rocksalt Sb_2Te_3. The arrow indicates the absence of antibonding interactions directly at E_F. E) The average local density of p states (LDOS) of Te atoms in rocksalt Sb_2Te_3 (supercell with 1008 atomic sites). Different curves correspond to Te atoms with different number of neighboring vacancies n_{Vac}. F) The inverse participation ratio (IPR), DOS, and the highest occupied molecular orbital (HOMO) state computed for the supercell of Sb_2Te_3 after full atomic relaxation. The HOMO state is represented by an isosurface (isovalue = 0.012 a.u., as in ref. [21]) rendered in blue and the atomic vacancies are highlighted with large, red spheres.

2006221 (3 of 10)

**ADVANCED
SCIENCE NEWS**

www.advancedsciencenews.com

**ADVANCED
MATERIALS**

www.advmat.de

Figure 3. A) XRD measurements of Sb_2Te_3 thin films ($\approx$460 nm thickness) annealed at different temperatures T_a from 80 to 300 °C and B) cycled resistivity measurement of the corresponding sample. The arrows indicate the progressive heating and cooling processes. The sample was held at each T_a over 30 min. C) Low-temperature transport measurements of two Sb_2Te_3 samples ($\approx$80 nm thickness) annealed at 140 and 300 °C. The temperature window for measurements is between 2 and 300 K.

configuration. Figure 2E shows a systematic change in LDOS near E_F: the higher the number of NN vacancies, the higher the LDOS of the Te atoms. This correlation suggests that, inside vacancy clusters (i.e., regions having a high concentration of vacancies), the p states of the Te atoms may form localized states with energies close to E_F. Intuitively, such clusters correspond to low-probability fluctuations in the vacancy distribution, which could induce localized states in the tail of the valence band. Upon relaxation, visible atomic distortions, on average $\approx$0.21 Å off the ideal sites, are observed, which open up a narrow bandgap (Figure 2D). The inverse participation ratio (IPR) is calculated to quantify the localization of the Kohn–Sham eigenstates.[21] In the infinite-size limit, the IPR is finite for localized states, whereas it is equal to zero for extended wave functions. For our finite-size models, the IPR values are nonzero even for delocalized states and equal approximately to $1/N$ (the inverse number of atoms). Nevertheless, our model size is sufficient to distinguish strongly localized from extended states. As shown in Figure 2F, the IPR values of the eigenstates near E_F are quite large. The IPR of the highest occupied molecular orbital (HOMO) state is $\approx$0.033, corresponding to a localized area covering $\approx$30 atoms. In the Supporting Information, we show that this value hardly changes upon increase of the system size up to 2520 atoms, indicating exponential localization (Figure S1, Supporting Information). We also include charge-density scans of this state along the x, y, and z axis for the largest 2520-atom models (Figures S2–S4, Supporting Information): the scans are performed by computing the electron density at several planes perpendicular to the relevant axis. The corresponding plots confirm the exponential decay of the charge density and, thus, the localized nature of the state. The electron wave function of the HOMO state is visualized in Figure 2F (blue surfaces) together with the atomic vacancies (red spheres). The electron wave function is indeed localized in a vacancy-rich area. This behavior is very similar to that seen in rocksalt $GeSb_2Te_4$.[21]

To validate our predictions experimentally, we perform diffraction and transport measurements. Two sets of Sb_2Te_3 thin films ($\approx$460 nm thickness) are prepared and treated under the same annealing conditions for the X-ray diffraction (XRD) and van der Pauw measurements. After deposition, the films are annealed in a tube furnace under an argon atmosphere at a rate

of 5 K min^{-1}, and are held at different annealing temperatures T_a for 30 min. As displayed in **Figure 3**A, the XRD pattern shows a clear cubic rocksalt feature for the samples annealed at 200 °C and below. A structural transformation takes place upon further thermal annealing. At 260 °C and above, the sample forms the rhombohedral phase. The temperature dependence of the resistivity ρ is shown in Figure 3B. Upon annealing, the resistivity continuously decreases due to progressive ordering in the crystal.[12] The sign of the temperature coefficient of the resistivity is negative ($d\rho/dT < 0$) for the samples annealed at 240 °C and below, but becomes positive ($d\rho/dT > 0$) at 260 °C and above, indicating a fundamental change from insulating-like to metallic-like transport character.

The samples show p-type transport behavior with large carrier concentrations of the order of 10^{19}–10^{20} cm^{-3}, which stems from similar self-doping effects as in Ge–Sb–Te alloys.[20,21] For further verification, we carry out transport experiments by cooling the Sb_2Te_3 thin films ($\approx$80 nm thickness) down to 2 K. As shown in Figure 3C, the resistivity of the rocksalt sample (annealed at 140 °C) shows a clear divergence in the low-temperature limit, whereas that of the rhombohedral sample (annealed at 300 °C) reaches a finite value when approaching 2 K, indicating metallic behavior.

In principle, several effects could lead to a low-temperature insulating phase, including a bandgap opening driven by charge order or Peierls distortion or a generic structural transition, as well as charge localization due to electron correlation effects (Mott transition). However, in Sb_2Te_3 and Ge–Sb–Te alloys, there is a large carrier concentration over the whole relevant temperature range stemming from self-doping. Furthermore, both the high- and low-temperature phase have similar bandgaps induced by Peierls-like distortions (in fact, the gap is slightly larger in the high-T phase). Finally, electron correlations are weak due to effective screening.[20] Signs of a soft Coulomb gap due electron correlations in the insulating regime[4] can only be observed at the lowest measurement temperatures (thus, in a very narrow energy range), where it manifests in a steeper temperature dependence of the resistivity.[22] Given the large carrier concentration, weak electron correlation effects, but strong atomic disorder, our interpretation of the data is that rocksalt-type Sb_2Te_3 is indeed an Anderson insulator. We note that variable range hopping and spin memory effects

**ADVANCED
SCIENCE NEWS**

www.advancedsciencenews.com

**ADVANCED
MATERIALS**

www.advmat.de
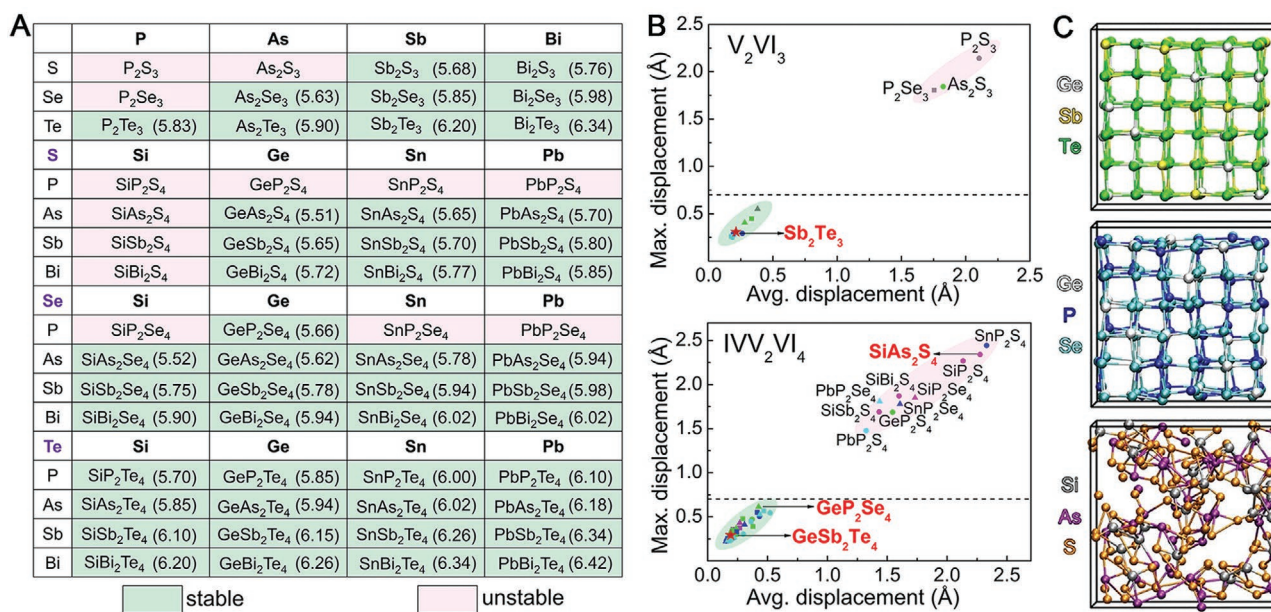
Figure 4. DFT screening over 60 rocksalt compounds. A) Structural stability of all the binary and ternary rocksalt chalcogenides, as defined by a maximum atomic displacement of ≈0.7 Å after structural relaxation. The calculated equilibrium lattice parameters (in Å) are given in parentheses. B) The maximum atomic displacement versus the average atomic displacement from the equilibrium position for ternary and binary compounds. The threshold value is marked by the dashed line at ≈0.7 Å. C) The relaxed structures of $GeSb_2Te_4$, GeP_2Se_4, and $SiAs_2S_4$ models, which are typical examples of stable alloys with small and large distortions, as well as unstable alloys.

were reported in Sb_2Te_3 thin films annealed below 170 °C very recently,[47] which also corroborates our interpretation.

Next, we carry out a systematic, DFT-based materials screening over all possible homologous V_2VI_3 and $IV_1V_2VI_4$ chalcogenides in the rocksalt type, where IV = Si, Ge, Sn, or Pb, V = P, As, Sb, or Bi, and VI = S, Se, or Te, giving 60 potential compositions. We generate cubic rocksalt models (3 × 3 × 3 supercells) for each composition, with statistical distributions of group IV and V atoms and vacancies on one sublattice, but a full occupation by the group VI atoms on the other. Structural and cell relaxation is performed for each composition on three independent models generated using a quasirandom number generator. In our rocksalt Sb_2Te_3 and $GeSb_2Te_4$ models, the maximum atomic displacement is ≈0.3 Å. As shown in **Figure 4**, in total we identify 9 binary and 38 ternary compounds with good structural stability in the rocksalt structure. These 47 stable compounds form the green shaded area in Figure 4B, defined by a maximum atomic displacement of ≈0.7 Å. The equilibrium lattice parameters of these compounds range from 5.63 Å for As_2Se_3 up to 6.34 Å for Bi_2Te_3 in binary compounds, and from 5.51 Å for $GeAs_2S_4$ up to 6.42 Å for $PbBi_2Te_4$ in ternary compounds (Figure 4A), increasing with the atomic radii of the constituent elements. The relaxed $GeSb_2Te_4$ and GeP_2Se_4 models are shown in Figure 4C, representing stable compounds with small and large distortions, respectively. The dynamical stability of these phases is verified by ab initio molecular dynamics (AIMD), heating up to 400 K for 100 ps (Methods Section; and Figure S5, Supporting Information).

Among the compositions that we studied, 3 binaries and 10 ternaries are unstable in the rocksalt structure (Figure 4A): upon relaxation, the underlying rocksalt-like structure is fully destroyed. One such example, $SiAs_2S_4$, is shown in Figure 4C.

No indication of long-range crystalline order is found in its radial distribution function (Figure S6, Supporting Information). The degree of structural instability can be quantified using the displacements of the relaxed atoms from the initial lattice sites (Figure 4B). For eight unstable compounds (3 binaries and 5 ternaries), the relaxed models show atomic displacements larger than half of the bond length, i.e., ≈1.5 Å, and an amorphous-like structure. As regards the remaining five ternary compounds, namely, $SiBi_2S_4$, SiP_2Se_4, SnP_2Se_4, PbP_2Se_4, and SnP_2S_4, the maximum displacement is between 0.8 and 1.5 Å upon DFT relaxation (Figure S7, Supporting Information). In particular, $SiBi_2S_4$ is very close to the stable green shaded area. However, these hypothetical compounds are dynamically unstable as revealed by AIMD: upon heating, the structures quickly turn amorphous-like, showing a much lower energy than the DFT relaxed ones (Figure S5, Supporting Information). These lower-energy atomic configurations are used for the displacement curve shown in Figure 4B, which marks a clear difference between stable and unstable compounds.

We compute several indicators to rationalize the results above. First, we calculate the ratio of the atomic radii of the elements occupying the two sublattices, i.e., r_V/r_{VI} for binary compounds, and max$(r_{IV}, r_V)/r_{VI}$ for ternaries. Second, we consider an orbital-based indicator—sp^3 mixing—that quantifies sp^3 like orbital mixing by projecting the DOS onto mixed levels.[48] These two quantities are computed on the basis of unrelaxed models, yet, they clearly categorize the relaxed and annealed models as stable (green) or unstable (red). The rocksalt structure becomes unstable for the compositions with both large sp^3 mixing and large atomic radius ratio, increasingly so when approaching the upper-right corner of the 2D part of the map in **Figure 5**. If only one of the two
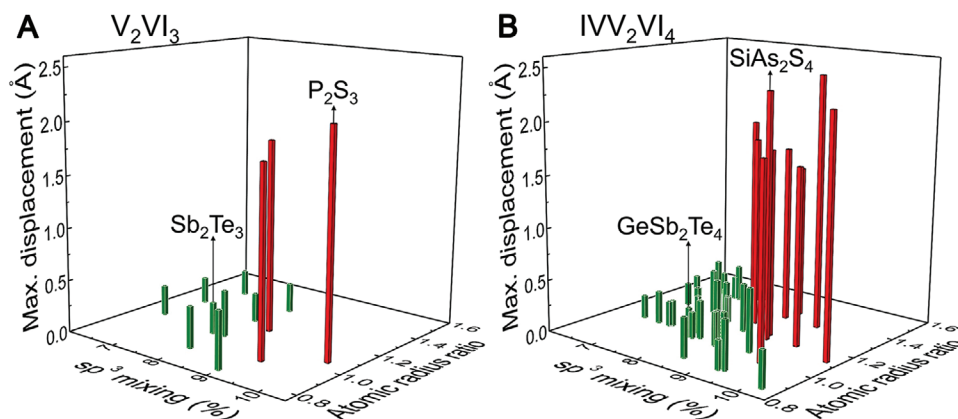
Figure 5. Structural stability analyses. A,B) The structural stability of binary (A) and ternary (B) rocksalt chalcogenides, quantified by the maximum displacement of atoms from their ideal lattice sites (the higher, the less stable) can be rationalized by the sp^3 mixing and atomic radius ratio. For ternary compounds, the larger atomic radius on the IV–V sublattice is used. The calculations are done using unrelaxed rocksalt structures. Stable and unstable compounds are indicated by green and red pillars. Typical unstable compounds, P_2S_3 and $SiAs_2S_4$, together with stable ones, Sb_2Te_3 and $GeSb_2Te_4$, are indicated by arrows.

indicators is large, the structure can still be stable. Except for a few compounds near the boundary region that become less well classified, the mapping remains qualitatively the same if the atomic radius ratio coordinate is replaced by the ionicity (Figure S8, Supporting Information), calculated by the difference between the Löwdin charges on the two sublattices.[48] Similarly, large ionicity in combination with strong atomic disorder weakens the rocksalt structure. Related bonding indicators derived from the electronic wavefunctions, defined as "electrons shared" and "electrons transferred,"[45] were used to map out MVB versus non-MVB behavior for a range of simple crystal structures. Interestingly, MVB is found in rhombohedral Sb_2Te_3 but not in orthorhombic Sb_2Se_3.[49] The interplay between disorder-induced phenomena and MVB remains to be further explored.

Next, we calculate the electronic structure for the 47 stable compounds. Large supercells containing 840 atoms (1008 sites including those of the vacancies) and 1680 atoms (1920 sites) are used for the binary and ternary compounds, respectively. These large system sizes are required to properly sample disorder on the IV–V sublattice in the ternary compounds. A quasirandom number generator is again used to create the three independent models for each compound, and the same three distributions of vacancies and group IV and V atoms are employed for different compounds. We focus on the energy region near E_F, which is relevant to transport properties. Specifically, we average the computed IPR over 21 eigenstates around E_F (HOMO ± 10) and over the three independent atomic configurations, as shown in **Figure 6**. In the perfect rocksalt-like models, localization is generally more significant for increasing atomic radius and
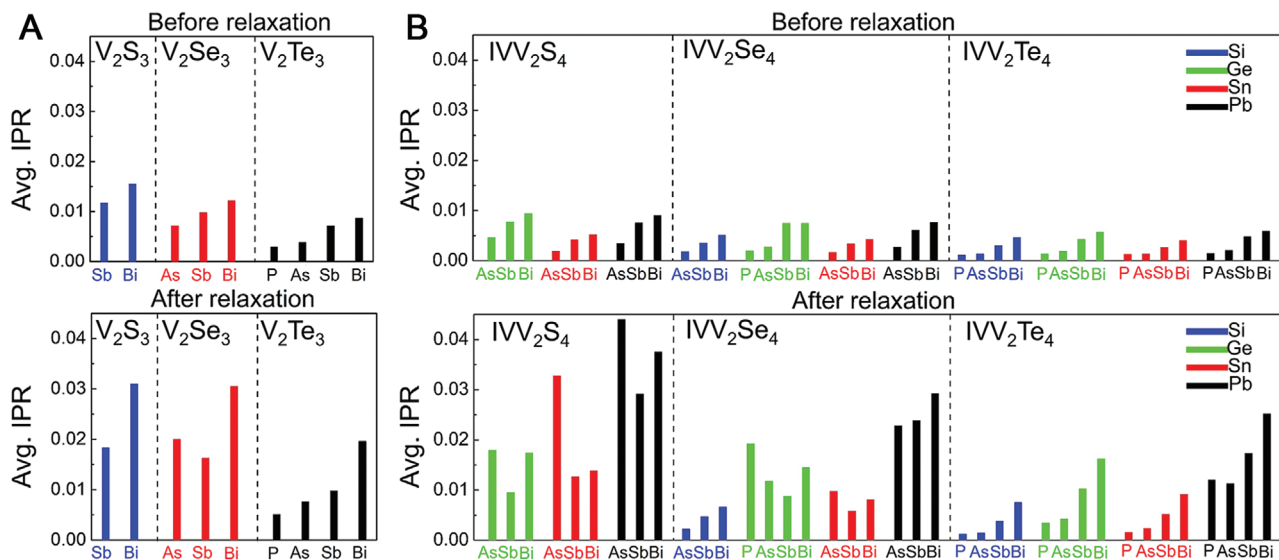
Figure 6. A,B) Localization properties of the 47 binary and ternary rocksalt-type compounds that are predicted to be viable by our analysis. IPR values were averaged over 21 Kohn–Sham eigenstates around the Fermi energy (HOMO ± 10) and over 3 independent atomic configurations for all stable binary (A) and ternary (B) rocksalt chalcogenides. The IPR data are provided both for the unrelaxed and relaxed rocksalt models. Only the 47 stable compounds indicated in Figure 4A are shown.

**ADVANCED
SCIENCE NEWS**

www.advancedsciencenews.com

**ADVANCED
MATERIALS**

www.advmat.de
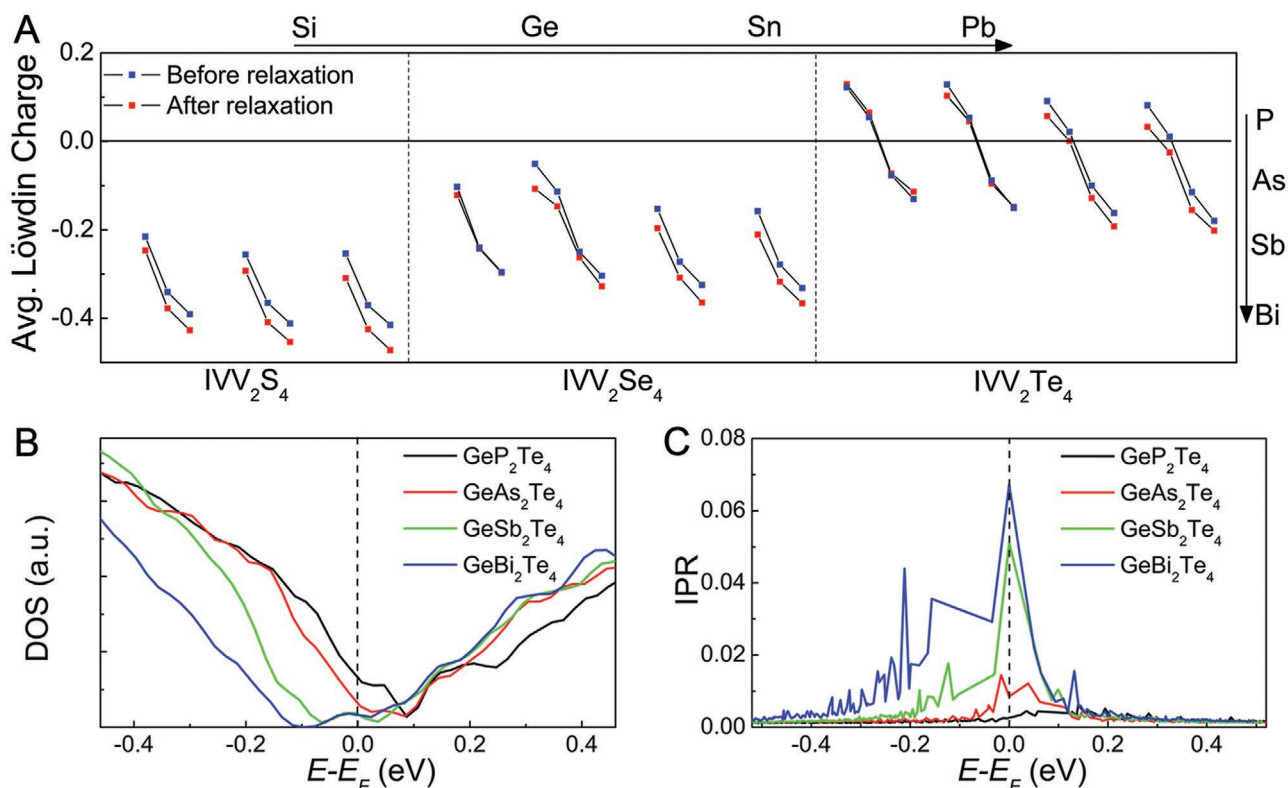
Figure 7. Löwdin charge and localization analyses. A) Average Löwdin charges for the group VI atoms in all 38 stable ternary compounds as shown in Figure 4A. For a given chalcogen element, series of points from left to right correspond to the series of group-IV elements (Ge → Pb for the sulfides, Si → Pb for the selenides and tellurides). Connected sets of points correspond to the series of group-V elements (As → Bi) or (P → Bi). The S and Se atoms serve as anions in all stable sulfides and selenides. The Te atoms serves as anions in most tellurides, but becomes cations in some cases with group IV and V elements of strong electronegativity. B) DOS and C) IPR of the relaxed rocksalt GeV_2Te_4 compounds, with V = P, As, Sb, and Bi. Note that these calculations used the GGA functional, which is known to underestimate the bandgap values. More accuarate hybrid functional calculations are presented in the Supporting Information.

decreasing electronegativity (EN) of the group V element, and for decreasing atomic radius and increasing EN of the group VI element. This indicates that localization is stronger for the more ionic solids characterized by large electron transfer. Upon relaxation, the atomic distortions lead to a further increase in IPR. The trend in localization remains qualitatively the same, despite some exceptions, for which relaxation effects are very strong. No obvious tendency concerning group IV elements is observed, neither before nor after geometry optimization. This is related to the fact these elements exhibit nonmonotonous trends in EN and, furthermore, their concentration is lower than that of the group V atoms. Interestingly, some of the models, such as SiP_2Te_4 and $SiAs_2Te_4$, do not display clear localization features, in spite of the strong disorder.

The EN difference between the elements and the resulting charge transfer is reflected by the distribution of the Löwdin charges, which are defined through a quantum-chemistry based electronic population analysis for partitioning the electrons between atoms.[50] In **Figure 7**A, we show average Löwdin charges on the group VI atoms for all ternary compounds. The most negative Löwdin charges are displayed by sulfides, followed by selenides. Remarkably, Te atoms exhibit a transition from positive to negative Löwdin charges upon changing from the most electronegative group V element, P, to the

least electronegative one, Bi. We take GeV_2Te_4 compounds with V = P, As, Sb, and Bi, for further analyses. As shown in Figure 7B and Figure S9 (Supporting Information), all four compounds are narrow-gap semiconductors. The energy gap increases from 0.23 eV for GeP_2Te_4 to 0.86 eV for $GeBi_2Te_4$. Approaching E_F, a clear increase in IPR is observed for all four compounds, yet the IPR values decrease as the atomic radius of the group V element decreases, while its EN increases (Figure 7C). In addition, the majority of Te atoms absorb electrons in $GeSb_2Te_4$ and $GeBi_2Te_4$, but lose electrons in GeP_2Te_4 and $GeAs_2Te_4$ (Figure S10, Supporting Information). The latter two compounds might display quite different transport characteristics as compared to the former two.

Qualitatively, we explain the trends in electron localization as follows. In all compounds studied, the p orbitals of the group VI atoms mainly contribute to the electronic states at the top of the valence band (note that this is valid even if the group VI elements act as cations, since the effective charge transfer is much less than 1 electron per atom and, thus, more valence electrons reside on the VI sites than on the IV–V sites; Figure 7A and Figure S8, Supporting Information). Furthermore, the larger the EN difference between the group V and VI elements, the stronger is the contribution of the latter elements to the states at the top of this band. Vacancy clusters can induce localization

of the states near the band edge, which are mainly constructed from the p orbitals of the undercoordinated group VI atoms, as shown in Figure 2D for Sb_2Te_3. Larger atomic radii of the group V atoms lead to larger lattice parameters (Figure 4A), whereas smaller radii of the group VI elements correspond to a smaller spatial extent of their p orbitals. Therefore, the two effects combined decrease the overlap between the p orbitals of the second- and fourth-nearest neighbor group VI atoms (the latter overlap is relevant if the two atoms are separated by a vacancy) and, thus, decrease the localization length. In addition, strong distortions upon relaxation further reduce the localization length and become the dominant factor for some of the compositions (Figure 6). The atomic distortions also open up an energy bandgap for all the stable binary and ternary compounds (Figure S9, Supporting Information), with an increase in gap size from tellurides (0.2–0.9 eV) to selenides (0.4–1.3 eV) and sulfides (0.9–1.8 eV). If self-doping effects were negligible, all these compounds would thus display semiconducting behavior. However, it is known that many of these alloys do exhibit p-type self-doping, which should make them Anderson insulators at low temperature (see Figure 1). Correlation effects could play a role in combination with disorder in those compounds where screening is less effective, leading to an Anderson–Mott insulator. It is also noted that the carrier type may change from p-type to n-type due to different self-doping effects in homologous chalcogenides,[33] which shall further enrich their portfolio of transport phenomena. For n-type systems, the localization of the states near the bottom of the conduction band becomes relevant.

Interestingly, some of these compounds—such as Sb_2Te_3, Bi_2Se_3, Bi_2Te_3, and Ge–Sb–Te—are topologically nontrivial in the layered rhombohedral phase due to strong spin–orbit coupling (SOC).[51–56] Our experiments (Figure 3) demonstrate that Sb_2Te_3 forms an Anderson-insulating rocksalt-like phase under low temperature annealing but gradually transforms into the rhombohedral phase upon high temperature annealing. Although rhombohedral Sb_2Te_3 exhibits metallic behavior due to the high concentration of hole carriers induced by self-doping, the surface states of thin films should be topologically protected against strong disorder. It is thus intriguing to elucidate the interplay between Anderson physics and topological physics in strongly-disordered rocksalt Sb_2Te_3, as well as the evolution of the electronic properties on the path toward the rhombohedral phase. In parallel to topological insulator (TI), the concept of topological Anderson insulator (TAI) has been proposed, where the bulk state is an Anderson insulator instead of a band insulator but the surface state is topologically protected.[57] In ref. [58], Anderson localization features have been observed in rhombohedral $(Bi_{1-x}Sb_x)_2Te_3$ TI films as the film thickness is reduced to a few quintuple layers, due probably to the effects of compositional disorder. Our results suggest that other sources of disorder, namely vacancy clusters, can also induce strong localization in heavy-element binary and ternary chalcogenides, in which SOC effects are typically strong. Our preliminary calculations indicate that the Anderson localization properties of rocksalt Sb_2Te_3 are not strongly affected by the inclusion of SOC. Further work, in particular the synthesis of single-crystalline rocksalt Sb_2Te_3 thin films and the experimental and theoretical investigation of surface states, is required to confirm whether rocksalt Sb_2Te_3 is a TAI or not.

In the context of practical applications, we demonstrated how DFT-based materials maps can be used to navigate the space of possible synthesis targets. One frontier in this regard is the development of multilevel high-density storage and neuro-inspired computing devices for Artificial Intelligence.[59] These technologies require single memory cells with a large number of stable resistance states. From our previous work,[60] we knew that Sb_2Te_3 can be switched between RESET amorphous and SET rocksalt states with a resistance window spanning about three orders of magnitude. Here we have demonstrated that the resistance of the SET state can potentially be extended by as much as another four orders of magnitude through tuning atomic disorder in the rocksalt phase, and our transport measurements of Sb_2Te_3 thin films showed 13 robust crystalline states with distinguishable resistance upon thermal annealing. On the other end of the spectrum, there are applications that call for high thermal stability, such as embedded memory[61] and nonvolatile photonic applications,[62] requiring increased stability of the RESET amorphous state. In general, selenides and sulfides are better glass-formers than tellurides.[63] For example, in ref. [64] the majority of Te atoms in $Ge_2Sb_2Te_5$ were substituted with Se, forming a $Ge_2Sb_2Se_4Te$ alloy, which increased the crystallization temperature by 50 °C. Besides, a wider energy bandgap is more suitable for low-loss photonic applications. Our map suggests that the optimization of the bandgap size and the amorphous stability by lighter-element compositions should proceed with an increase in either sp^3 mixing or atomic radius ratio. An increase in both factors is not recommended, however, because it would destabilize the rocksalt phase.

In summary, we carried out a computational screening over homologues of $GeSb_2Te_4$ and Sb_2Te_3 in the rocksalt structure. We identified 9 binary group V chalcogenides and 38 ternary group IV and V chalcogenides that could sustain such structure with significant atomic disorder, most of which are expected to display Anderson localization and disorder-governed transport properties in the presence of (self-)doping. Away from the stability border, we predict that thousands more compositions could be systematically explored upon gradual isoelectronic substitution in V_2VI_3 and IVV_2VI_4, such as $(As_{1-x}Sb_x)_2Te_3$, $Ge(Bi_{1-x}Sb_x)_2Te_4$, $SnSb_2(Se_{1-x}Te_x)_4$, and many other ternary, quaternary, quinary, and even more complex solid solutions. Similarly, multiple stoichiometries along the pseudobinary line ($IV_2V_2VI_5$, $IV_3V_2VI_6$, IVV_4VI_7 and others), with varying vacancy concentration, could be considered. Our work vastly expands the family of possible chalcogenide Anderson insulators and can help identify suitable compounds for phase-change applications with tailored transport properties and degree of disorder. It shall therefore serve as a strong stimulus in further exploration of Anderson physics in disordered chalcogenide materials.

Methods Section

Materials and Characterization: Sb_2Te_3 thin films of 460 and 80 nm thickness using stoichiometric targets on Si (100) substrates with a 1 µm SiO_2 layer for electrical transport measurements and on glass for X-ray diffraction were sputtered. A capping layer of ≈20 nm $(ZnS)_{80}(SiO_2)_{20}$ was added in situ to protect the samples from oxidation. The crystallized thin films were polycrystalline and the crystal structure was characterized by grazing-incidence X-ray diffraction on Sb_2Te_3 films of both 460 and

80 nm thickness, which yielded comparable results. For the electrical measurements, both Sb_2Te_3 devices in van der Pauw (460 nm) and Hall bar (80 nm) geometry have been fabricated by an initial contact metal pad evaporation followed by the application of shadow masks during the sputtering process. The Hall bar measurements were performed in a temperature range from 2 to 300 K by applying low excitation currents on the order of 0.005–1 µA in order to prevent Joule heating in the samples.

Computational Details: The Vienna Ab initio Simulation Package (VASP) was used[65] to carry out the structural relaxation with both atomic positions and lattice parameters fully relaxed for the $3 \times 3 \times 3$ cubic supercell models, which have 180 and 189 atoms in the binary and ternary compounds, respectively. The Perdew–Burke–Ernzerhof (PBE) functional[66] based on the generalized gradient approximation (GGA) was used and the energy cutoff was set to 500 eV. COHP and Löwdin charge analyses were carried out using a projection onto atom-centered orbitals as implemented in LOBSTER.[67,68] The energy gap size was determined using the Heyd–Scuseria–Ernzerhof hybrid functional.[69] Furthermore large supercells containing 840 (1008) and 1680 (1920) atoms (lattice sites) were considered to calculate localization properties for the binary and ternary rocksalt chalcogenides. The calculations were performed using the CP2K package.[70] Scalar-relativistic Goedecker[71] pseudopotentials and the PBE functional were employed with the cutoff of 300 Ry. Ab initio molecular dynamics simulations were also carried out on the basis of $3 \times 3 \times 3$ cubic supercell models using CP2K. Each compound was heated up to 400 K in 40 ps, annealed at 400 K for 50 ps and then quenched to 0 K in 10 ps. The time step for the simulations was 2 fs. The Brillouin zone was sampled at the Γ point only. If not mentioned otherwise, the calculations were done using the GGA functional.

Supporting Information

Supporting Information is available from the Wiley Online Library or from the author.

Acknowledgements

Conflict of Interest

The authors declare no conflict of interest.

Keywords

[1] P. W. Anderson, *Phys. Rev.* **1958**, *109*, 1492.
[2] N. F. Mott, *J. Non-Cryst. Solids* **1968**, *1*, 1.
[3] E. Abrahams, P. W. Anderson, D. C. Licciardello, T. V. Ramakrishnan, *Phys. Rev. Lett.* **1979**, *42*, 673.
[4] B. I. Shklovskii, A. L. Efros, *Electronic Properties of Doped Semiconductors*, Springer, Berlin, Germany **1984**.
[5] T. Giamarchi, H. J. Schulz, *Phys. Rev. B* **1988**, *37*, 325.
[6] D. Belitz, T. R. Kirkpatrick, *Rev. Mod. Phys.* **1994**, *66*, 261.
[7] D. M. Basko, I. L. Aleiner, B. L. Altshuler, *Ann. Phys.* **2006**, *321*, 1126.
[8] D. S. Wiersma, P. Bartolini, A. Lagendijk, R. Righini, *Nature* **1997**, *390*, 671.
[9] G. Roati, C. D'Errico, L. Fallani, M. Fattori, C. Fort, M. Zaccanti, G. Modugno, M. Modugno, M. Inguscio, *Nature* **2008**, *453*, 895.
[10] I. Bloch, J. Dalibard, S. Nascimbène, *Nat. Phys.* **2012**, *8*, 267.
[11] J. Billy, V. Josse, Z. Zuo, A. Bernard, B. Hambrecht, P. Lugan, D. Clement, L. Sanchez-Palencia, P. Bouyer, A. Aspect, *Nature* **2008**, *453*, 891.
[12] T. Schwartz, G. Bartal, S. Fishman, M. Segev, *Nature* **2007**, *446*, 52.
[13] W. Zhang, R. Mazzarello, M. Wuttig, E. Ma, *Nat. Rev. Mater.* **2019**, *4*, 150.
[14] S. Raoux, W. Welnic, D. Ielmini, *Chem. Rev.* **2010**, *110*, 240.
[15] D. Lencer, M. Salinga, M. Wuttig, *Adv. Mater.* **2011**, *23*, 2030.
[16] A. Sebastian, M. Le Gallo, R. Khaddam-Aljameh, E. Eleftheriou, *Nat. Nanotechnol.* **2020**, *15*, 529.
[17] Z. Zhang, Z. Wang, T. Shi, C. Bi, F. Rao, Y. Cai, Q. Liu, H. Wu, P. Zhou, *InfoMat* **2020**, *2*, 261.
[18] J. Feldmann, N. Youngblood, C. D. Wright, H. Bhaskaran, W. H. P. Pernice, *Nature* **2019**, *569*, 208.
[19] K. Konstantinou, F. C. Mocanu, T. H. Lee, S. R. Elliott, *Nat. Commun.* **2019**, *10*, 3065.
[20] T. Siegrist, P. Jost, H. Volker, M. Woda, P. Merkelbach, C. Schlockermann, M. Wuttig, *Nat. Mater.* **2011**, *10*, 202.
[21] W. Zhang, A. Thiess, P. Zalden, R. Zeller, P. H. Dederichs, J. Y. Raty, M. Wuttig, S. Blügel, R. Mazzarello, *Nat. Mater.* **2012**, *11*, 952.
[22] H. Volker, P. Jost, M. Wuttig, *Adv. Funct. Mater.* **2015**, *25*, 6390.
[23] P. Jost, H. Volker, A. Poitz, C. Poltorak, P. Zalden, T. Schaefer, F. Lange, R. M. Schmidt, B. Hollaender, M. R. Wirtssohn, M. Wuttig, *Adv. Funct. Mater.* **2015**, *25*, 6399.
[24] W. Zhang, M. Wuttig, R. Mazzarello, *Sci. Rep.* **2015**, *5*, 13496.
[25] B. Zhang, W. Zhang, Z.-J. Shen, Y.-J. Chen, J.-X. Li, S.-B. Zhang, Z. Zhang, M. Wuttig, R. Mazzarello, E. Ma, X.-D. Han, *Appl. Phys. Lett.* **2016**, *108*, 191902.
[26] A. Lotnyk, T. Dankwort, I. Hilmi, L. Kienle, B. Rauschenbach, *Nanoscale* **2019**, *11*, 10838.
[27] T.-T. Jiang, X.-D. Wang, J.-J. Wang, Y.-X. Zhou, D.-L. Zhang, L. Lu, C.-L. Jia, M. Wuttig, R. Mazzarello, W. Zhang, *Acta Mater.* **2020**, *187*, 103.
[28] V. Bragaglia, F. Arciprete, W. Zhang, A. M. Mio, E. Zallo, K. Perumal, A. Giussani, S. Cecchi, J. E. Boschker, H. Riechert, S. Privitera, E. Rimini, R. Mazzarello, R. Calarco, *Sci. Rep.* **2016**, *6*, 23843.
[29] S. Privitera, A. M. Mio, E. Smecca, A. Alberti, W. Zhang, R. Mazzarello, J. Benke, C. Persch, F. La Via, E. Rimini, *Phys. Rev. B* **2016**, *94*, 094103.
[30] A. Lotnyk, M. Behrens, B. Rauschenbach, *Nanoscale Adv.* **2019**, *1*, 3836.
[31] M. Cutler, N. F. Mott, *Phys. Rev.* **1969**, *181*, 1336.
[32] J. Reindl, H. Volker, N. P. Breznay, M. Wuttig, *npj Quantum Mater.* **2019**, *4*, 57.
[33] T. Schäfer, P. M. Konze, J. D. Huyeng, V. L. Deringer, T. Lesieur, P. Müller, M. Morgenstern, R. Dronskowski, M. Wuttig, *Chem. Mater.* **2017**, *29*, 6749.
[34] P. Nukala, R. Agarwal, X. Qian, M. H. Jang, S. Dhara, K. Kumar, A. T. Johnson, J. Li, R. Agarwal, *Nano Lett.* **2014**, *14*, 2201.
[35] A. Edwards, A. Pineda, P. Schultz, M. Martin, A. Thompson, H. Hjalmarson, C. Umrigar, *Phys. Rev. B* **2006**, *73*, 045210.
[36] T. Matsunaga, R. Kojima, N. Yamada, K. Kifune, Y. Kubota, Y. Tabata, M. Takata, *Inorg. Chem.* **2006**, *45*, 2235.

[37] S. Maier, S. Steinberg, Y. Cheng, C. F. Schon, M. Schumacher, R. Mazzarello, P. Golub, R. Nelson, O. Cojocaru-Miredin, J. Y. Raty, M. Wuttig, *Adv. Mater.* **2020**, *32*, 2005533.

[38] C. Chen, P. Jost, H. Volker, M. Kaminski, M. Wirtssohn, U. Engelmann, K. Krüger, F. Schlich, C. Schlockermann, R. P. S. M. Lobo, M. Wuttig, *Phys. Rev. B* **2017**, *95*, 094111.

[39] B. J. Kooi, M. Wuttig, *Adv. Mater.* **2020**, *32*, 1908302.

[40] F. Rao, K. Ding, Y. Zhou, Y. Zheng, M. Xia, S. Lv, Z. Song, S. Feng, I. Ronneberger, R. Mazzarello, W. Zhang, E. Ma, *Science* **2017**, *358*, 1423.

[41] Y. Zheng, M. Xia, Y. Cheng, F. Rao, K. Ding, W. Liu, Y. Jia, Z. Song, S. Feng, *Nano Res.* **2016**, *9*, 3453.

[42] R. Dronskowski, P. E. Blöchl, *J. Phys. Chem.* **1993**, *97*, 8617.

[43] M. Wuttig, D. Lusebrink, D. Wamwangi, W. Welnic, M. Gillessen, R. Dronskowski, *Nat. Mater.* **2007**, *6*, 122.

[44] M. Wuttig, V. L. Deringer, X. Gonze, C. Bichara, J. Y. Raty, *Adv. Mater.* **2018**, *30*, 1803777.

[45] J. Y. Raty, M. Schumacher, P. Golub, V. L. Deringer, C. Gatti, M. Wuttig, *Adv. Mater.* **2019**, *31*, 1806280.

[46] I. Ronneberger, Z. Zanolli, M. Wuttig, R. Mazzarello, *Adv. Mater.* **2020**, *32*, 2001033.

[47] I. Korzhovska, H. Deng, L. Zhao, Y. Deshko, Z. Chen, M. Konczykowski, S. Zhao, S. Raoux, L. Krusin-Elbaum, *npj Quantum Mater.* **2020**, *5*, 39.

[48] M. Esser, V. L. Deringer, M. Wuttig, R. Dronskowski, *Solid State Commun.* **2015**, *203*, 31.

[49] Y. Cheng, O. Cojocaru-Mirédin, J. Keutgen, Y. Yu, M. Küpers, M. Schumacher, P. Golub, J.-Y. Raty, R. Dronskowski, M. Wuttig, *Adv. Mater.* **2019**, *31*, 1904316.

[50] P. O. Löwdin, *J. Chem. Phys.* **1950**, *18*, 365.

[51] H. Zhang, C.-X. Liu, X.-L. Qi, X. Dai, Z. Fang, S.-C. Zhang, *Nat. Phys.* **2009**, *5*, 438.

[52] D. Hsieh, Y. Xia, D. Qian, L. Wray, F. Meier, J. Dil, J. Osterwalder, L. Patthey, A. Fedorov, H. Lin, A. Bansil, D. Grauer, Y. Hor, R. Cava, M. Hasan, *Phys. Rev. Lett.* **2009**, *103*, 146401.

[53] Y. Jiang, Y. Wang, M. Chen, Z. Li, C. Song, K. He, L. Wang, X. Chen, X. Ma, Q.-K. Xue, *Phys. Rev. Lett.* **2012**, *108*, 016401.

[54] J. Kim, J. Kim, S.-H. Jhi, *Phys. Rev. B* **2010**, *82*, 201312(R).

[55] J. Tominaga, A. V. Kolobov, P. Fons, T. Nakano, S. Murakami, *Adv. Mater. Inter.* **2014**, *1*, 1300027.

[56] B. Sa, J. Zhou, Z. Sun, J. Tominaga, R. Ahuja, *Phys. Rev. Lett.* **2012**, *109*, 096802.

[57] H. M. Guo, G. Rosenberg, G. Refael, M. Franz, *Phys. Rev. Lett.* **2010**, *105*, 216601.

[58] J. Liao, Y. Ou, X. Feng, S. Yang, C. Lin, W. Yang, K. Wu, K. He, X. Ma, Q. K. Xue, Y. Li, *Phys. Rev. Lett.* **2015**, *114*, 216601.

[59] W. Zhang, E. Ma, *Mater. Today* **2020**, *41*, 156.

[60] K. Ding, J. Wang, Y. Zhou, H. Tian, L. Lu, R. Mazzarello, C. Jia, W. Zhang, F. Rao, E. Ma, *Science* **2019**, *366*, 210.

[61] P. Cappelletti, R. Annunziata, F. Arnaud, F. Disegni, A. Maurelli, P. Zuliani, *J. Phys. D: Appl. Phys.* **2020**, *53*, 193002.

[62] M. Wuttig, H. Bhaskaran, T. Taubner, *Nat. Photonics* **2017**, *11*, 465.

[63] C. Lin, C. Rüssel, S. Dai, *Prog. Mater. Sci.* **2018**, *93*, 1.

[64] Y. Zhang, J. B. Chou, J. Li, H. Li, Q. Du, A. Yadav, S. Zhou, M. Y. Shalaginov, Z. Fang, H. Zhong, C. Roberts, P. Robinson, B. Bohlin, C. Ríos, H. Lin, M. Kang, T. Gu, J. Warner, V. Liberman, K. Richardson, J. Hu, *Nat. Commun.* **2019**, *10*, 4279.

[65] G. Kresse, J. Furthmüller, *Phys. Rev. B* **1996**, *54*, 11169.

[66] J. P. Perdew, K. Burke, M. Ernzerhof, *Phys. Rev. Lett.* **1996**, *77*, 3865.

[67] R. Nelson, C. Ertural, J. George, V. L. Deringer, G. Hautier, R. Dronskowski, *J. Comput. Chem.* **2020**, *41*, 1931.

[68] S. Maintz, V. L. Deringer, A. L. Tchougréeff, R. Dronskowski, *J. Comput. Chem.* **2013**, *34*, 2557.

[69] J. Heyd, G. E. Scuseria, M. Ernzerhof, *J. Chem. Phys.* **2006**, *124*, 219906.

[70] J. Hutter, M. Iannuzzi, F. Schiffmann, J. VandeVondele, *WIREs Comput. Mol. Sci.* **2014**, *4*, 15.

[71] S. Goedecker, M. Teter, J. Hutter, *Phys. Rev. B* **1996**, *54*, 1703.

2006221 (10 of 10)